Micromagnetic behavior of electrodeposited cylinder arrays

C. A. Ross,[1,*] M. Hwang,[1] M. Shima,[1] J. Y. Cheng,[1] M. Farhoud,[2] T. A. Savas,[3] Henry I. Smith,[2] W. Schwarzacher,[4] F. M. Ross,[5] M. Redjdal,[6] and F. B. Humphrey[6]

[1]*Department of Materials Science and Engineering, Massachusetts Institute of Technology, Cambridge, Massachusetts 02139*

[2]*Department of Electrical Engineering and Computer Science, Massachusetts Institute of Technology, Cambridge, Massachusetts 02139*

[3]*Department of Physics, Massachusetts Institute of Technology, Cambridge, Massachusetts 02139*

[4]*H. H. Wills Physics Laboratory, University of Bristol, Bristol BS8 1TL, United Kingdom*

[5]*IBM T. J. Watson Research Center, Yorktown Heights, New York 10598*

[6]*Department of Electrical and Computer Engineering, Boston University, Boston, Massachusetts 02215*

(Received 27 July 2001; published 28 March 2002)

Arrays of cylindrical magnetic particles have been made using interference lithography combined with electrodeposition. The cylinders are made from Ni, Co, CoP, or CoNi, with diameters of 57–180 nm, aspect ratios of 0.4–3, and array periods of 100–200 nm. The remanent states of the cylinders correspond to single-domain ''flower'' states or to magnetization vortices depending on the particle size and aspect ratio. Experimental data are in good agreement with a magnetic-state map calculated using a three-dimensional micromagnetic model, which shows the remanent state as a function of particle size and aspect ratio. The interactions between the particles, and their switching-field distribution, have been quantified.

DOI: 10.1103/PhysRevB.65.144417 PACS number(s): 75.75.+a, 75.60.Ch

I. INTRODUCTION

There has been extensive interest in the magnetic properties of small (sub-100 nm) ferromagnetic particles or elements, due to their possible applications in patterned magnetic recording media and other magnetic or magnetoelectronic devices.[1,2] The magnetic behavior of such elements depends on their size relative to the magnetic exchange length $\lambda_{ex}=\sqrt{(A)}/M_s$ (expressed in cgs units), where A is the exchange constant and M_s the saturation moment. For ferromagnetic metals, λ_{ex} is typically in the range 6–20 nm. Elements of sub-100 nm dimensions are usually too small to support well-developed multidomain structures at remanence, but they are too large to be uniformly magnetized, hence their magnetization states typically contain nonuniformities such as magnetization vortices, or variations in the magnetization direction exist at their surfaces or edges. These nonuniform magnetization states lead to complex magnetic switching behavior that is not well described by the coherent rotation model. Although in some cases, agreement with coherent rotation[3] or curling[4,5] models has been obtained, generally it is found that measured switching fields are lower than model predictions[6,7] or show a different dependence on diameter,[8] the activation volume is smaller than the physical volume of the particle,[4,9–11] or switching statistics do not follow the Néel model[12] indicating a more complex magnetization reversal process. Other effects such as magnetostriction also cause deviations from the curling model.[10,13]

Computational micromagnetic models have, therefore, been used to improve understanding of both the remanent states and the switching behavior of small particles. This was initially done for the two-dimensional case of thin-film magnetic elements[14,15] but in recent years, lithography, magnetic characterization, and computational techniques have improved to the point that it is now possible to compare three-dimensional model predictions directly to experimental data gathered from individual particles or arrays of particles, revealing the effects of microstructure, edge roughness, and size variations on magnetic behavior, and giving some insight into the reversal mechanism and the effects of interactions between particles. Three-dimensional micromagnetic studies have usually concentrated on the switching behavior of single-domain particles with high aspect ratio, for instance, magnetic-tape particles[16] or particles made by electrodeposition into porous membranes or templates prepared lithographically.[7,17] Additionally, calculations of remanent states of ideal particle shapes such as cubes or cuboids have been made, as a function of size, shape, and anisotropy,[18–20] and nonuniform magnetization states in cylinders have been examined.[21–23] There have only been a few direct comparisons of computational remanence studies with experimental data.[24]

This paper presents a detailed comparison between the remanent states of arrays of low-aspect ratio cylindrical particles and a three-dimensional micromagnetic calculation. The transition between ''single domain'' and more complex remanent magnetization states deduced from hysteresis loops and magnetic images is compared with the predictions of the micromagnetic model, and good agreement is found. The interactions between particles within the array and their switching-field distributions have been quantified.

II. SAMPLE FABRICATION, STRUCTURAL CHARACTERIZATION AND MODELING

The cylinder arrays are fabricated by electrodeposition into templates made by interference lithography or achromatic interference lithography.[24–26] These methods are chosen because they are capable of exposing large area (several square centimeter) substrates with deep-submicron features in a patterning process that is much faster than electron-beam lithography. Both lithography methods rely on the interference between two laser beams to produce a fringe pattern that is used to expose a trilevel resist layer. Two perpendicular exposures are used to define a square array of holes in the

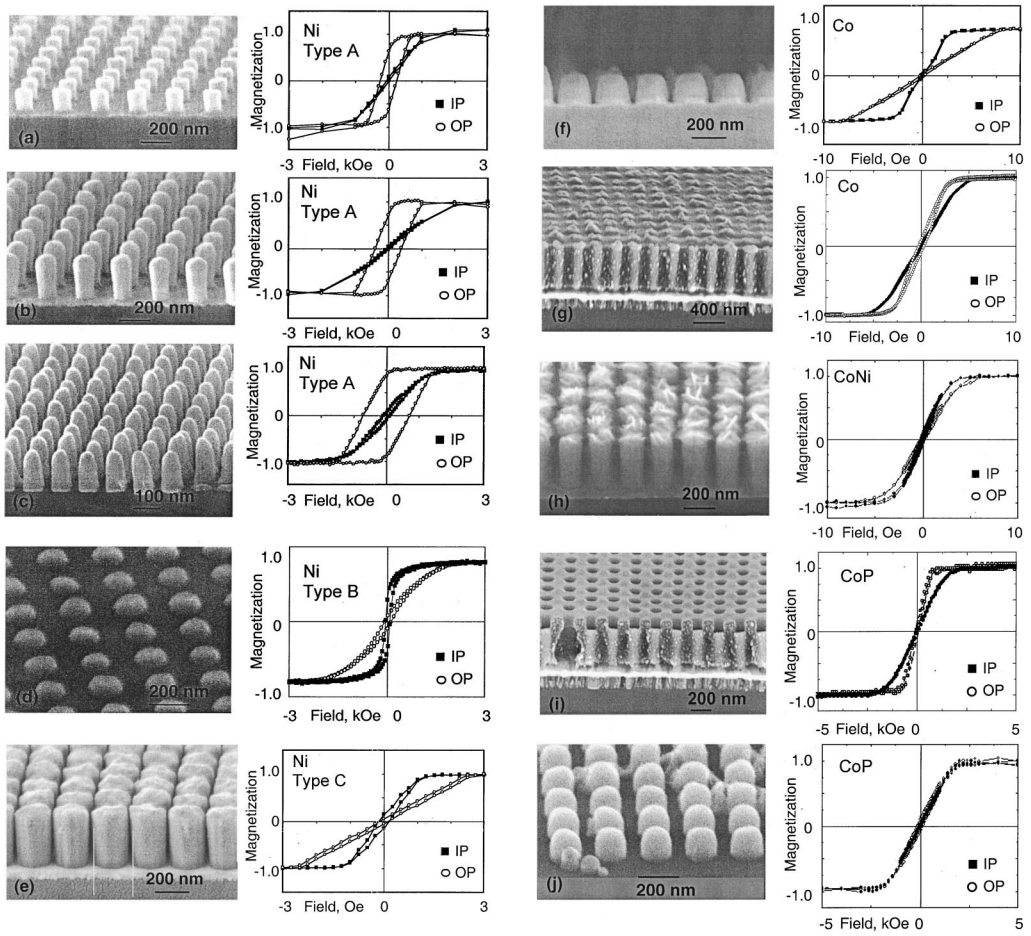

FIG. 1. Scanning electron micrographs of selected cylinder arrays of Ni, Co, CoP, and CoNi, and corresponding hysteresis loops. The field is applied either in-plane (IP, solid points) or out-of-plane (OP, open points). Additional samples are shown in Refs. 28 and 40. The magnetization is normalized to the saturation magnetization of the sample.

top resist layer. A negative resist is used for improved process latitude.[27] The hole pattern is transferred from the resist through an intermediate mask into an underlying 300–400 nm thick antireflective coating layer using reactive ion etching to give holes with straight sidewalls, which form the mold for the deposition of the cylinder arrays. The interference lithography system produces patterns with period 200 nm and above, while the achromatic-interference lithography system produces patterns with period 100 nm. The diameter of the holes in the template is controlled through the exposure dose, and was varied in the range of 0.4–0.9 times the array period.

The templates are made on silicon wafers coated with a thin evaporated conductive layer consisting of 5 nm Ti or Cr followed by 5–20 nm Au. The cylinder arrays are fabricated by electrodeposition from aqueous electrolytes as described previously.[28] Co and Ni are deposited from sulfamate electrolytes from a commercial vendor (MacDermid). CoNi pyrophosphate and CoP phosphate electrolytes were mixed from salts. The area to be electroplated, 1–10 cm^2, is defined using a tape or photoresist mask. Depositions are carried out galvanostatically, except for CoNi alloys that are deposited potentiostatically. After deposition, the antireflective coating template could be removed using an oxygen reactive ion etch to enable the cylinders to be imaged by scanning electron microscopy.

The microstructure of the samples was assessed using x-ray diffraction, transmission electron microscopy, and scanning electron microscopy. Compositions of alloys were determined by energy dispersive x-ray analysis or x-ray photoelectron spectroscopy using appropriate standards such as Co_2P powder in the case of CoP samples. Magnetic characterization was carried out using an ADE vibrating sample magnetometer or a Princeton alternating gradient magnetometer, and a Digital Instruments magnetic force microscope (MFM). Figure 1 shows representative scanning electron micrographs and hysteresis loops of several cylinder arrays. The cylinders have straight sides, with a slight taper in some cases due to an increase in the hole diameter through the thickness of the template.

Nickel samples were polycrystalline with a (111) fcc preferred orientation. From transmission electron microscopy [Figs. 2(a) and 2(b)], the as-deposited grain size was 10–20 nm, smaller than the cylinder diameter. However, annealing the smaller cylinders such as the sample shown in Fig. 1(c) during the reactive ion etch could result in recrystallization, and the final microstructure then consisted of single-crystal cylinders with occasional grain boundaries or stacking faults

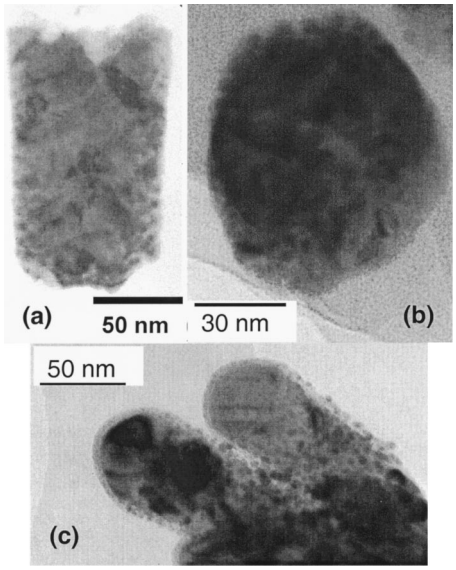

FIG. 2. Transmission electron micrographs of electrodeposited Ni (a) polycrystalline Ni cylinder similar to Fig. 1(b), side view; (b) top view, indicating an equiaxed crystal structure with grain size of 10 nm. (c) Single-crystal Ni cylinders similar to Fig. 1(c), side view. The horizontal features in the right-hand cylinder are stacking faults or twin boundaries. The cylinders have a 5-nm oxide coating, and small circular features around their edges are redeposited gold from their conductive base layer.

visible [Fig. 2(c)]. Co samples deposited from the sulfamate electrolyte had a weak (0001) preferred orientation. $Co_{100-x}Ni_x$ was deposited from an electrolyte containing different ratios of Co and Ni ions such that $[Co^{2+}]+[Ni^{2+}]=0.2$ molar. As the percentage of Co in the electrolyte increased from 15 to 75 %, the Co content of the deposit also increased linearly, varying between 60 at. % and 98.1 at. %. The alloy was polycrystalline with random crystallographic orientation and had an hcp structure across the composition range. In the case of $Co_{100-x}P_x$, samples were made with $11<x<26$ at. % by varying the current density. The alloy was polycrystalline for low x but was amorphous or nanocrystalline for $x>15$ at. %. CoP cylinders had concave top surfaces as deposited, but the heating experienced during removal of the template caused the cylinder structures to smooth out into spherical shapes as shown in Fig. 1(j).

The remanent states of isolated cylindrical particles were calculated using a three-dimensional micromagnetic model.[24,29] The particle was discretized into cubic cells to approximate the cylindrical shape, with 31 cells aross the diameter. The cell size was always kept below $0.5\lambda_{ex}$. The starting state consisted of a uniform magnetization state parallel or perpendicular to the cylinder axis, or a circumferential vortex. The Landau-Lifschitz-Gilbert equations were then solved to find the equilibrium magnetization direction within each cell, taking into account magnetostatic interactions, nearest-neighbor exchange interactions, and any external fields or local anisotropies. The calculation used an exchange constant of 10^{-6} erg cm^{-1} and a gyromagnetic ratio of 0.0179 Oe^{-1} ns^{-1}, and a damping constant of 1 to ensure rapid convergence.

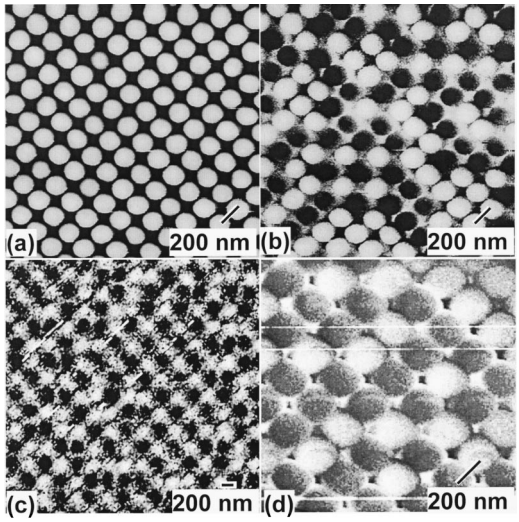

FIG. 3. (a) Topographic, and (b) magnetic image of an area of the Ni sample of Fig. 1(b) in its as-deposited condition. Each cylinder has the same height in (a), but shows as a dark or light spot in (b) corresponding to ''up'' or ''down'' magnetization. (c) Lower magnification image of the same sample after ac demagnetization. Areas of ''checkerboard'' pattern are visible. (d) MFM image of the CoP sample of Fig. 1(i) after removing the template. In (a), (b), and (d) the rows of cylinders run diagonally across the picture while in (c) they run horizontally. The scale bars are printed parallel to the rows.

III. MAGNETIC PROPERTIES OF ARRAYS

A. Hysteresis loops and remanent states

A total of 34 samples of different materials were prepared, with heights of 66–400 nm, diameters of 57–180 nm and aspect ratios R (=height/diameter) of 0.4–3. For the Co and Ni samples, the saturation moment M_s is consistently lower than that of the pure metals, presumably due to the codeposition of impurities into the films (both sulfamate solutions contain proprietary additives to reduce grain size). The Ni samples had $M_s=320$ emu cm^{-3}, 0.66 times that of pure Ni. For Co samples, $M_s=1100$ emu cm^{-3}, 0.77 times that of pure Co. For $Co_{100-x}P_x$, M_s decreases approximately linearly as x increases, extrapolating to zero at $x=33$ at. % in agreement with previous data.[30] The CoP cylinder arrays had moments in the range 280–585 emu cm^{-3}. For CoNi alloys, M_s increases with Co content, and falls between 750 and 1050 emu cm^{-3} for the samples reported here.

Three types of hysteresis loops were identified, as shown in Fig. 1. High aspect ratio, low diameter Ni samples have a high coercivity, trapezoidal (''sheared'') hysteresis loop in the out-of-plane direction, while the in-plane direction shows low coercivity and remanence characteristic of a hard axis. This was labeled as type *A* [Figs. 1(a)–1(c)]. For these samples, MFM shows each cylinder as either a dark or a light spot (Fig. 3). This is consistent with each cylinder behaving like a magnetic dipole oriented perpendicular to the plane.

In contrast, two low-aspect-ratio Ni samples ($R=0.41$ and 0.74) show hysteresis loops characteristic of an easy axis in plane, with a hard axis parallel to the cylinder height. This is labeled as type *B* [Fig. 1(d)]. The symmetry of the cylindrical

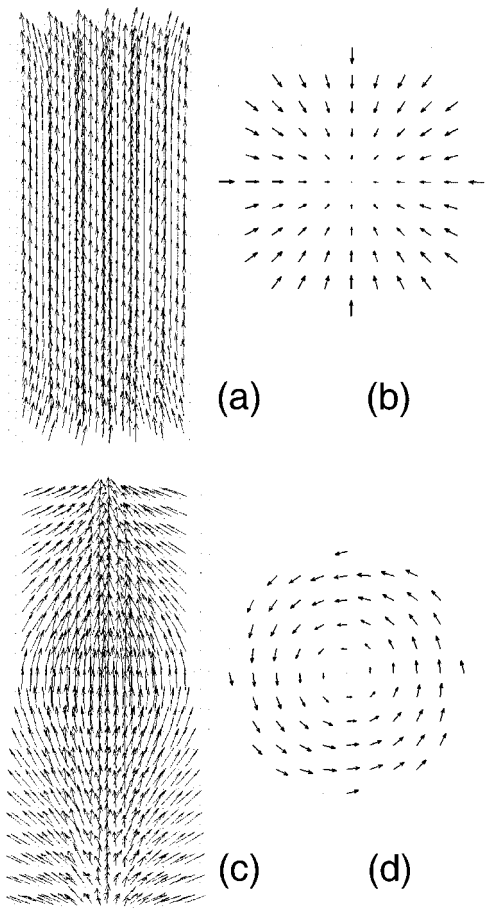

FIG. 4. Calculated remanent magnetization distributions in cylindrical particles. (a) Side view and (b) bottom face of a cylinder of aspect ratio $R=2.1$ and diameter $d=2.61\lambda_{ex}$, showing a flower state. (c) Side view and (d) top face of cylinder with $R=2.1$, and $d=6.1\lambda_{ex}$, showing a vortex state. The arrow lengths in (b) and (d) are plotted at different scales for clarity.

particles would suggest that there should be an easy plane of magnetization, with zero in-plane coercivity, but the samples do have significant in-plane coercivity, presumably due to pinning of the magnetization by inhomogeneities or surface roughness as it rotates in plane. Similar results have been obtained for low-aspect-ratio evaporated particles.[24]

The majority of the samples, including the larger diameter Ni samples and all the Co and CoNi samples, show hysteresis in which both in-plane and out-of-plane magnetization directions have low coercivity and remanence, identified as type *C* [Figs. 3(e)–(h)]. The field required to saturate the magnetization in either direction depends on the aspect ratio and spacing of the cylinders. Higher aspect ratio or more widely separated cylinders have lower out-of-plane saturation fields. MFM images of some samples were recorded and show little contrast, implying flux closure within the particles that leads to small external fields and low remanence.

To interpret these results, a three-dimensional micromagnetic simulation of the remanent state of an isolated cylindrical particle was carried out. The simulation was used to identify regimes of behavior for small particles, i.e., those with aspect ratio less than 3 and diameters less than about $6\lambda_{ex}$.

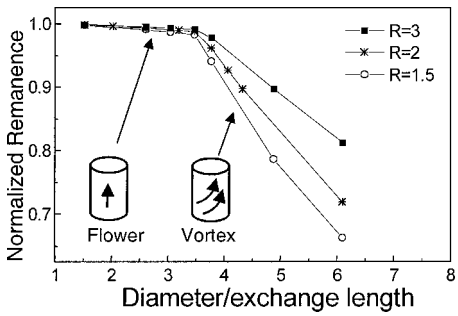

FIG. 5. Calculated remanence along the cylinder axis as a function of cylinder diameter, for three different aspect ratios *R*. The flower state has a remanence close to 1, which decreases as the vortex develops.

In the case of high-aspect-ratio particles ($R>0.9$), for small diameters a ''flower-state'' magnetization is found to be the lowest energy state. The magnetization is parallel to the axis of the particle, except near the top and bottom surfaces where it spreads radially, and the axial remanence is close to 1 [Figs. 4(a) and 4(b)]. As the diameter increases, a gradual transition to a ''vortex'' state occurs. The magnetization adopts a helical structure, starting at the ends of the particle, while the magnetization at the center of the particle remains oriented primarily along the axis [Figs. 4(c) and 4(d)]. The remanence drops with increasing diameter as the magnetization tilts away from the axis. Remanence decreases more slowly with diameter for higher aspect ratio cylinders because the region of tilted magnetization is confined to a smaller volume fraction of the particles. The variation in axial remanence with diameter is illustrated in Fig. 5. The flower-vortex transition is defined as the diameter at which circumferential tilt was *first* observed. This occurred at a diameter of approximately $3.5\lambda_{ex}$ for aspect ratios of 1–3. Cubic[19] and cuboidal[18] particles show similar flower-vortex transitions with increasing size.

As the aspect ratio decreases, there is a transition from the out-of-plane flower state to an in-plane flower state at an aspect ratio below 0.9, in agreement with a value of 0.9065 calculated for a uniformly magnetized cylinder.[23,31] Particles with $R<0.9$ show a transition from an in-plane flower to a vortex state with increasing diameter, which occurs at larger diameters as *R* decreases. The low-aspect-ratio vortex consists of circumferential magnetization at the perimeter with an out-of-plane component at the center of the cylinder. As the vortex state develops, the exchange energy increases and the magnetostatic energy decreases. The stable state was determined by comparing the total energy of the two configurations. The calculated energy and hence the onset of the vortex depends to some extent on the discretization cell size; all these calculations were based on 31 cells across the diameter of the cylinder. As the cylinder diameter increases, more complex states were obtained containing domain walls.

Figure 6 shows the boundaries of the in-plane flower, out-of-plane flower, and vortex regions as a function of diameter and aspect ratio. The boundary between the in-plane and out-of-plane flower states is shown at $R=0.9$.[23,31] The boundary between the out-of-plane flower and vortex states

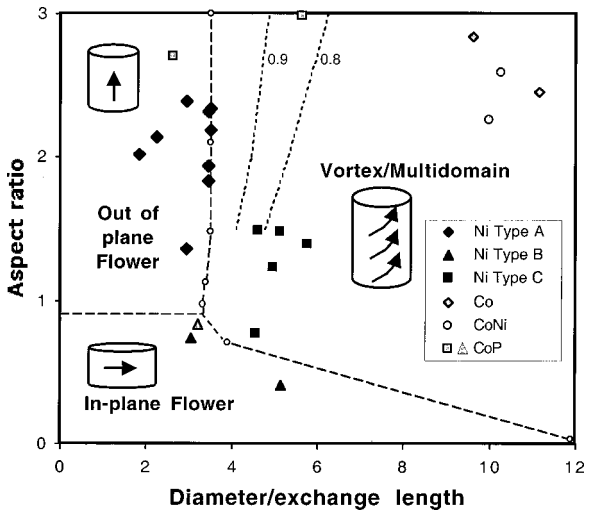

FIG. 6. A map showing the boundaries between the out-of-plane and in-plane flower remanent states and the vortex remanent states calculated as a function of aspect ratio and cylinder diameter. The out-of-plane flower to vortex transition is plotted as the diameter at which circumferential magnetization was first observed at the ends of the cylinder. The out-of-plane flower state has an axial remanence of 1, which decreases as the diameter increases and the vortex develops. Two contours of constant remanence (0.8 and 0.9) are shown as dotted lines for high-aspect-ratio vortex-state cylinders. Superposed on the plot are data points corresponding to the electrodeposited samples. The Ni samples are shown in three groups based on their hysteresis loop shapes; these show excellent agreement with the calculated boundaries. The Co and CoNi samples all fall well within the vortex region and have low remanence. The CoP particles indicated by square symbols have high remanence while the triangular point has low remanence, also in agreement with the model.

is plotted at the diameter where circumferential tilt was first observed, though significantly the remanence is very close to 1 at this diameter and decreases only slowly with increasing diameter. High-aspect-ratio vortex-state particles can, therefore, still have a high remanence, as shown by two contours of equal remanence indicated on the figure. The boundary between the in-plane flower and vortex states is plotted based on only two data points.

This ''magnetic-state diagram'' can now be compared with the experimentally determined remanent states of the cylinder arrays. Data points corresponding to the samples are superposed on Fig. 6, based on the physical dimensions of the samples and the exchange length calculated from the measured saturation moment of each sample. Each data point is coded according to the hysteresis loop type. For the Ni samples, there is a good correlation between type-*A* loops and the out-of-plane flower-state region, type-*B* loops and the in-plane flower-state region, and type-*C* loops and the vortex region. The CoNi and Co particles are all well within the vortex region and all show type-*C* loops.

The quantitative correspondence between the data points and the magnetic-state diagram supports the following interpretation of the remanent configurations of the particles. The type-*A* loops represent out-of-plane flower-state particles with high coercivity and remanence. The shear of the out-of-plane hysteresis loop is a result of magnetostatic interactions between the particles, as will be discussed below. The type-*B* loops represent particles with an in-plane flower state. Individual particles have high remanence but interactions tilt the magnetizations in plane and reduce the net remanence of the array. The type-*C* loops represent particles that contain more complex configurations such as vortices causing partial flux closure, which reduces the remanence of individual particles to a greater degree as the particles become larger. These particles are expected to have low coercivity because small applied fields can move the vortex through the particle.

The CoP samples all showed type-*C* loops with low remanence and coercivity. Three of them were investigated further using MFM. Two samples with high aspect ratio, indicated with square symbols on Fig. 6, both showed dipolar contrast [Fig. 3(d)] indicating that the individual particles have high remanence, as expected from the magnetic-state map. However, the coercivity of the individual particles is so low that interactions dominate the shape of the hysteresis loops, so the overall remanence of the array is small due to self-demagnetization. A third sample of lower aspect ratio, indicated with a triangular symbol on Fig. 6, showed preferred in-plane magnetization but no detectable contrast in MFM, which is consistent with low out-of-plane remanence.

Several groups have reported the fabrication of electrodeposited cylindrical particles of Ni, Fe, or NiFe that show dipolar MFM images similar to Fig. 3. For example, (25–50)-nm-diameter Ni (Ref. 32) and 10–14-nm-diameter Fe (Ref. 4) showed dipolar contrast. Chou and co-workers observed dipolar states in 50–70-nm-diameter Ni but no contrast in 110-nm-diameter cylinders, suggesting multidomain states at the higher diameter.[33,34] 140-nm-diameter NiFe cylinders were described as being in a vortex configuration.[35] Tall Ni cylinders of 200 nm diameter also commonly show MFM contrast[36,37] that is consistent with development of a vortex with significant remanence in a high-aspect-ratio particle. In all these reports, the transition from flower state to vortex or multidomain states, and the high remanence of elongated particles, agree with the interpretation of the magnetic state of the particles that is presented here.

The presence of uniaxial anisotropy additionally influences the remanent state of small particles. To assess its importance, the effect of uniaxial anisotropy K_u added parallel to the cylinder axis was modeled. For high aspect ratios R, anisotropy stabilizes the out-of-plane flower state to higher diameters. Figure 7 shows how the flower-vortex transition varies with normalized anisotropy ($Q=K_u/2\pi M_s$) in particles with $R=1.5-3$. For comparison, the uniaxial magnetocrystalline anisotropy of hcp Co corresponds to $Q=0.35$. At this value of Q, the transition occurs at $16.8\lambda_{ex}$ for $R=1.5$, increasing slightly with aspect ratio. Therefore any anisotropy present in the particles, due, for instance, to a preferred crystal orientation, can significantly affect the remanent state. Such effects have been seen in evaporated Ni and Co particles,[24] and may contribute to the high remanence in 120-nm-diameter evaporated Ni particles,[38,39] but are not believed to be important in the electrodeposited cylinders reported here. In the polycrystalline Ni samples, the grains are small and equiaxed, and the magnetocrystalline anisotropy is

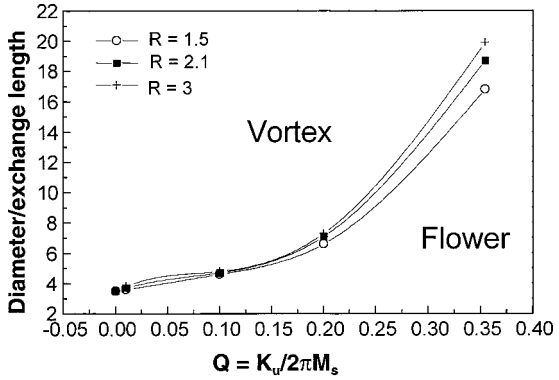

FIG. 7. The flower-vortex transition as a function of axial anisotropy, for cylinders of aspect ratio $R=1.5-3$. The anisotropy is normalized to $Q=K_u/2\pi M_s$. Axial anisotropy stabilizes the vortex state to larger diameters.

weak, leading to negligible effects on remanent state. The CoP samples are amorphous or nanocrystalline, and the CoNi is polycrystalline with no preferred orientation. The only samples studied here where magnetocrystalline anisotropy may change the remanent state are the Co samples, where the weak preferred orientation leads to a net axial anisotropy equal to about a tenth of the magnetocrystalline anisotropy of single crystal Co. However, according to Fig. 7, the particles are still large enough to be in the vortex state.

B. Interactions between particles

The importance of interparticle magnetostatic interactions can be estimated by comparing the nearest-neighbor interaction field H_i to the switching field of an individual cylinder H_c. H_i can be calculated straightforwardly for saturated particles by treating them as magnetic dipoles or prisms. If we consider a square array of parallel identical dipoles with magnetization perpendicular to the plane, the total field acting on any given dipole, obtained by summing the inverse-cube dipolar field from all other particles in the array, is $9H_i$. Hence the parameter $9H_i/H_c$ gives an indication of how strongly interacting an array is. If $9H_i/H_c>1$, then the fields from neighboring particles can be large enough to reverse the magnetization of a particle in the array leading to a remanence less than 1. In contrast, if $9H_i/H_c<1$ then the saturated magnetic state is stable at remanence. Such behavior has been observed experimentally.[40]

Out-of-plane hysteresis loops can be modeled by assuming that the array consists of magnetostatically interacting cylinders. Each cylinder is assumed to have a square hysteresis loop but there is a spread in their switching fields.[39–43] To fit to the measured data, the spacing, diameter, height, average switching field, and moment of the cylinders in a 12×12 array are assigned values measured from the sample, and hysteresis loops are calculated; the only fitting parameter is the standard deviation of switching fields σ. This model gives excellent fits to cylinder arrays with type-*A* hysteresis loops. Figure 8 shows results of the model including fits to the samples of Figs. 1(b) and 1(c) both for the major loop and the virgin curve following ac demagnetization. This supports the assumption that individual cylinders have nearly square hysteresis loops, which is consistent with the high remanence calculated for flower-state particles, unlike the case for conical evaporated particles.[24] The lowest magnetostatic energy configuration of a square array is to have each cylinder alternately magnetized up or down. When imaged in MFM, this resembles a checkerboard pattern of alternating light and dark features. In the more strongly interacting ar-

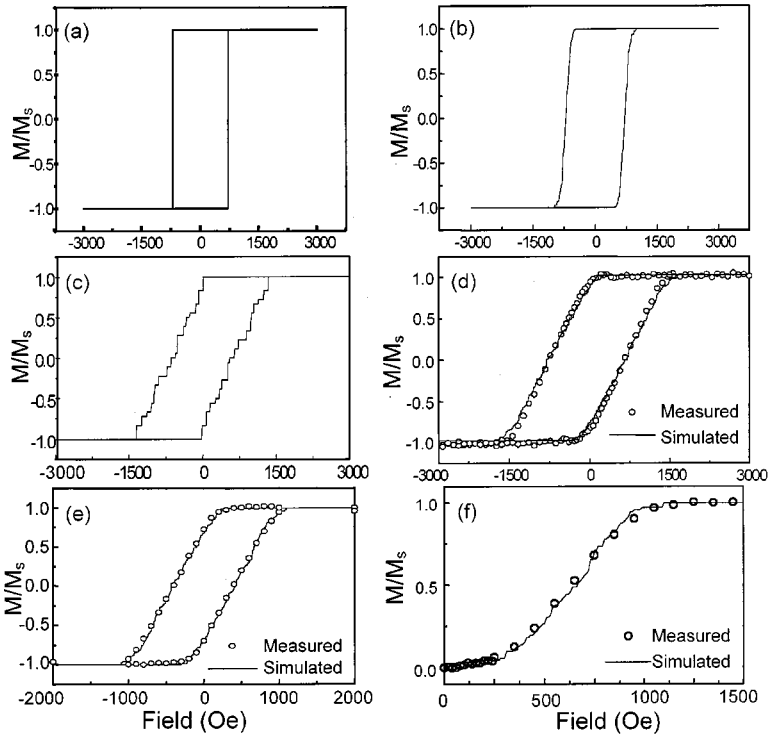

FIG. 8. Out-of-plane hysteresis loops for arrays of type-*A* particles, modeled using parameters from the sample of Fig. 1(c). (a) Calculated hysteresis loop in the case that the particles all have the same switching field of 710 Oe and there are no interactions; (b) the case that the particles have a Gaussian distribution of switching fields with $\sigma=15$ Oe, but there are no interactions; (c) the case that the particles interact but all have the same switching field; (d) the case including both interactions and the switching-field distribution, which gives a good fit to the measured hysteresis loop of sample 1(c). (e) A fit to sample 1(b) with $\sigma=100$ Oe. (f) A calculated virgin curve for sample 1(b), using the same parameters as in (e), which compares well with experimental data.

rays, we have found that this pattern forms spontaneously over small areas of the sample,[40] but it can be formed in more weakly interacting arrays by ac demagnetizing the sample, then imaging it with a low-moment MFM tip to avoid disturbing the pattern. An MFM image of the sample of Fig. 1(b), which exhibits a correlated checkerboard pattern over lengths as large as 1 μm, is shown in Fig. 4(c).

In the case of very strong interactions, the out-of-plane magnetization of the cylinders reorients to an in-plane direction. Reorientation occurs more readily at low aspect ratios, and its onset has been calculated for saturated cylinder arrays.[31] However, reorientation was not observed in this experiment because none of the type-*A* arrays was sufficiently closely spaced.

For type-*B* particles, a more complex interaction model is needed to account for the possibility of rotation of the magnetization in plane and the different angles between the moments of neighboring particles.[44–46] The simpler case of elliptical thin-film elements with in-plane magnetization, which have an in-plane uniaxial easy axis, has, however, been treated using a modified interaction model.[42] Type-*C* arrays cannot easily be fitted using the dipolar interaction model because the particles are not saturated at all fields. Their behavior is dominated by interactions because H_c is small; we find that more closely spaced arrays show a higher out-of-plane saturation field that is consistent with stronger interactions.

C. The switching field distribution

Control of the switching field is critical in any device application of particle arrays. The spread in switching fields of the particles arises from two causes: the effects of magnetostatic interactions, and intrinsic variability between the particles. These two factors cause the hysteresis loop of the array to be nonsquare, even though individual particles may have square hysteresis loops.

Intrinsic variability between particles arises from small variations in size, shape, or the statistical effects of the grains in polycrystalline particles. The intrinsic variability, expressed by the standard deviation σ of the switching-field distribution, can be extracted from the fit to the shape of the hysteresis loops as discussed above, but we have found that the quality of the fit is not highly sensitive to the value of σ chosen. A better estimate of σ can be obtained by the process of imaging the array by MFM in a varying applied field. Figure 9 shows examples of such data for a type-*A* Ni sample. An increasing magnetic field was applied by bringing a permanent magnet towards the sample. The total applied field is the sum of the field from the permanent magnet plus that of the MFM tip. [The tip field is calibrated by using it to image an ac demagnetized sample, then counting the number of ''up'' and ''down'' cylinders, calculating the net magnetization, and comparing this with the virgin curve to determine what field the tip produced.] For each particle that switches at a given applied field, the magnetization states of its neighbors are known so the true switching field of the particle can be found. For the sample of Fig. 1(c), which has

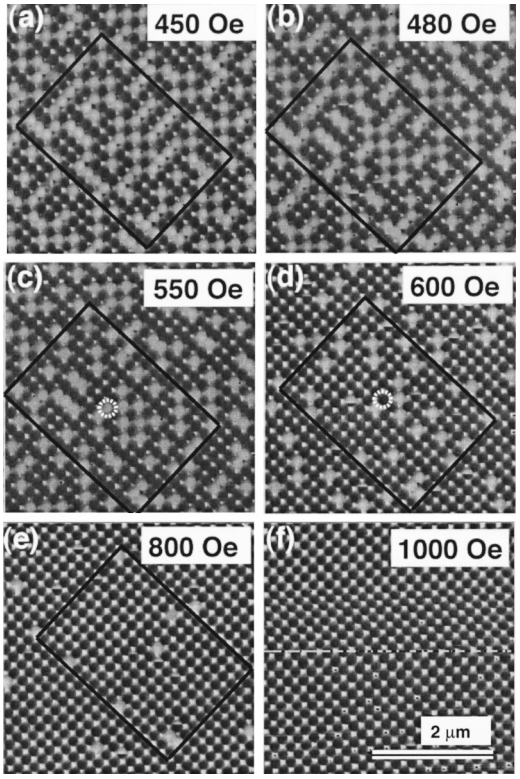

FIG. 9. MFM images of the Ni sample of Fig. 1(b) under different fields applied out of plane. The rectangle encloses the same area of 16×11 particles. The particles reverse successively as the field increases; one is outlined to show it reversing.

$H_c = 710$ Oe, we found $\sigma = 105$ Oe, which is mainly attributed to variations in cylinder diameter.[47] Clearly, for applications involving small magnetic particles, σ must be minimized by control of both the lithographic processing and the microstructure of the particles.

IV. CONCLUSIONS

The magnetic behavior of arrays of electrodeposited cylinders with diameters of 57–180 nm and aspect ratios of 0.4–3 has been investigated. For aspect ratios (height/diameter) greater than 0.9, the smaller diameter particles show high remanence parallel to the cylinder axis and hysteresis loops characteristic of an array of ''single-domain'' particles that interact magnetostatically. As the particle size increases, the remanence and coercivity decrease and the existence of vortex or multidomain states is inferred. This behavior is in excellent agreement with the results of a micromagnetic model, which predicts a gradual transition from a flower to a vortex remanent state and corresponding decrease in axial remanence as the diameter increases. In contrast, low-aspect-ratio particles have an easy magnetization plane parallel to their base, and the flower-vortex transition occurs at larger diameters as the aspect ratio decreases.

Such particle arrays have applications in patterned magnetic recording media. This requires the particles to be single

domain with significant axial remanence: this can be achieved in small particles even at modest aspect ratios, and is promoted by the presence of axial anisotropy. Interactions shear the hysteresis loops, and can dominate the overall hysteresis loop of the array in the case of low coercivity particles such as CoP_x. In patterned media applications, magnetostatic interactions must be sufficiently small to avoid array self-demagnetization, and the intrinsic switching-field distribution must be minimized by control of lithography and microstructure.

ACKNOWLEDGMENTS

The authors acknowledge the assistance of A. Tkaczyk, J. Parrochon, and W. Escoffier in sample preparation, and support from the National Science Foundation Grant No. DMR 9871539.

*Email address: caross@mit.edu

[1] P. R. Krauss, P. Fischer, and S. Y. Chou, J. Vac. Sci. Technol. B **12**, 3639 (1994).
[2] S. S. P. Parkin, K. P. Roche, M. G. Samant, P. M. Rice, R. B. Beyers, R. E. Scheuerlein, E. J. O'Sullivan, S. L. Brown, J. Buccigano, D. W. Abraham, Y. Lu, M. Rooks, P. L. Trouilloud, R. A. Wanner, and W. J. Gallagher, J. Appl. Phys. **85**, 5828 (1999).
[3] W. Wernsdorfer, E. Bonet Orozco, K. Hasselbach, A. Benoit, B. Barbara, N. Demoncy, A. Loiseau, H. Pascard, and D. Mailly, Phys. Rev. Lett. **78**, 1791 (1997).
[4] S. Wirth, M. Field, D. D. Awschalom, and S. von Molnar, Phys. Rev. B **57**, R14 028 (1998).
[5] S. Wirth, J. J. Heremans, S. von Molnar, M. Field, K. L. Campman, A. C. Gossard, and D. D. Awschalom, IEEE Trans. Magn. **34**, 1105 (1998).
[6] R. O'Barr and S. Schultz, J. Appl. Phys. **81**, 5458 (1997).
[7] C. Seberino and H. N. Bertram, IEEE Trans. Magn. **33**, 3055 (1997).
[8] R. O'Barr, M. Lederman, S. Schultz, W. Xu, A. Scherer, and R. J. Tonucci, J. Appl. Phys. **79**, 5303 (1996).
[9] W. Wernsdorfer, B. Doudin, D. Mailly, K. Hasselbach, A. Benoit, J. Meier, J. P. Ansermet, and B. Barbara, Phys. Rev. Lett. **77**, 1873 (1996).
[10] S. Pignard, G. Goglio, A. Radulescu, L. Piraux, S. Dubois, A. Declemy, and J. L. Duvail, J. Appl. Phys. **87**, 824 (2000).
[11] J. E. Wegrowe, D. Kelly, A. Franck, S. E. Gilbert, and J. P. Ansermet, Phys. Rev. Lett. **82**, 3681 (1999).
[12] M. Lederman, S. Schultz, and M. Ozaki, Phys. Rev. Lett. **73**, 1986 (1994).
[13] J. Meier, B. Doudin, and J. P. Ansermet, J. Appl. Phys. **79**, 6010 (1996).
[14] J. F. Smyth, S. Schultz, D. Fredkin, D. P. Kern, S. A. Rishton, H. Schmid, M. Cali, and T. R. Koehler, J. Appl. Phys. **69**, 5262 (1991).
[15] G. A. Gibson and S. Schultz, J. Appl. Phys. **73**, 4516 (1993).
[16] C. Seberino and H. N. Bertram, J. Appl. Phys. **85**, 5543 (1999).
[17] R. Ferré, K. Ounadjela, J. M. George, L. Piraux, and S. Dubois, Phys. Rev. B **56**, 14 066 (1997).
[18] M. E. Schabes and H. N. Bertram, J. Appl. Phys. **64**, 1347 (1988).
[19] W. Rave, K. Fabian, and A. Hubert, J. Magn. Magn. Mater. **190**, 332 (1998).
[20] A. J. Newell and R. T. Merrill, J. Appl. Phys. **84**, 4394 (1998).
[21] A. S. Arrott and T. L. Templeton, Physica B **233**, 259 (1997).
[22] A. Hubert and W. Rave, J. Magn. Magn. Mater. **184**, 67 (1998).
[23] A. Aharoni, J. Appl. Phys. **68**, 2892 (1990).
[24] C. A. Ross, M. Farhoud, M. Hwang, H. I. Smith, M. Redjdal, and F. B. Humphrey, J. Appl. Phys. **89**, 1310 (2001).
[25] C. A. Ross, H. I. Smith, T. A. Savas, M. Schattenburg, M. Farhoud, M. Hwang, M. Walsh, M. C. Abraham, R. J. Ram, J. Vac. Sci. Technol. B **17**, 3168 (1999).
[26] C. A. Ross, R. Chantrell, M. Hwang, M. Farhoud, T. A. Savas, Y. Hao, H. I. Smith, F. M. Ross, M. Redjdal, F. B. Humphrey, Phys. Rev. B **62**, 14 252 (2000).
[27] M. Farhoud, J. Ferrera, T. J. Lochtefeld, T. E. Murphy, M. L. Schattenburg, J. M. Carter, C. A. Ross, and H. I. Smith, J. Vac. Sci. Technol. B **17**, 3182 (1999).
[28] M. Shima, M. Hwang, M. Farhoud, T. A. Savas, A. Tkaczyk, H. I. Smith, C. A. Ross, W. Schwarzacher, Proc.-Electrochem. Soc. **PV2000-29**, 111 (2001).
[29] M. Redjdal and F. B. Humphrey, J. Appl. Phys. **79**, 6464 (1996).
[30] D. Pan and D. Turnbull, J. Appl. Phys. **45**, 2406 (1974).
[31] K. Y. Guslienko, S. B. Choe, and S. C. Shin, Appl. Phys. Lett. **76**, 3609 (2000).
[32] K. Nielsch, R. B. Wehrspohn, S. F. Fischer, H. Kronmuller, J. Barthel, J. Kirschner, and U. Gosele, MRS Symposia Proceedings No. 636 (Materials Research Society, Pittsburgh, 2001).
[33] B. Cui, W. Wu, L. Kong, X. Sun, and S. Y. Chou, J. Appl. Phys. **85**, 5534 (1999).
[34] S. Y. Chou, Proc. IEEE **85**, 652 (1997).
[35] M. Zenger, W. Breuer, M. Zolfl, R. Pulwey, J. Raabe, and D. Weiss, IEEE Trans. Magn. **37**, 2094 (2001).
[36] R. O'Barr, S. Y. Yamamoto, S. Schultz, W. Xu, and A. Scherer, J. Appl. Phys. **81**, 4730 (1997).
[37] J. Wong, A. Scherer, M. Todorovic, and S. Schultz, J. Appl. Phys. **85**, 5489 (1999).
[38] G. Meier, M. Kleiber, D. Grundler, D. Heitmann, and R. Wiesendanger, Appl. Phys. Lett. **72**, 2168 (1998).
[39] D. Grundler, G. Meier, K. B. Broocks, C. Heyn, and D. Heitmann, J. Appl. Phys. **85**, 6175 (1999); **88**, 6957(E) (2000).
[40] M. Hwang, M. C. Abraham, T. A. Savas, H. I. Smith, R. J. Ram, and C. A. Ross, J. Appl. Phys. **87**, 5108 (2000).
[41] G. Zheng, M. Pardavi-Horvath, and G. Vertesy, J. Appl. Phys. **81**, 5591 (1997).
[42] M. Hwang, M. Farhoud, Y. Hao, M. Walsh, T. A. Savas, H. I. Smith, and C. A. Ross, IEEE Trans. Magn. **36**, 3173 (2001).
[43] L. C. Sampaio, E. C. H. P. Sinnecker, G. R. C. Cernicchiaro, M. Knobel, M. Vazquez, and J. Velazquez, Phys. Rev. B **61**, 8976 (2000).
[44] K. Y. Guslienko, Appl. Phys. Lett. **75**, 394 (1999).
[45] R. L. Stamps and R. E. Camley, Phys. Rev. B **60**, 11 694 (1999).
[46] V. Russier, J. Appl. Phys. **89**, 1287 (2001).
[47] M. C. Abraham, H. Schmidt, T. A. Savas, H. I. Smith, C. A. Ross, and R. J. Ram, J. Appl. Phys. **89**, 5667 (2001).